Advanced Functional Materials

ADVANCED FUNCTIONAL MATERIALS
www.afm-journal.de

RESEARCH ARTICLE OPEN ACCESS

MAGTWIST: A Magnetically-Driven Rotary Actuator Using a Traveling-Wave With Integrated Stiffness Tunability

Simon Frieler[1] | Jean-Paul P.M. de Vries[2] | Sarthak Misra[1,3] | Venkatasubramanian Kalpathy Venkiteswaran[1]

[1]Surgical Robotics Laboratory, Department of Biomechanical Engineering, University of Twente, Enschede, The Netherlands | [2]Division of Vascular Surgery, Department of Surgery, University Medical Center Groningen, University of Groningen, Groningen, The Netherlands | [3]Surgical Robotics Laboratory, Department of Biomaterials and Biomedical Technology, University of Groningen City and University Medical Centre Groningen, Groningen, The Netherlands

Correspondence: Simon Frieler (s.frieler@utwente.nl)

Received: 10 October 2025 | **Revised:** 3 December 2025 | **Accepted:** 9 December 2025

Keywords: magnetic actuation | minimally invasive surgery | rotary actuators | shape-memory polymers | traveling waves | variable stiffness

ABSTRACT

Robotic systems in confined environments rely on compact and dexterous actuators. In minimally invasive surgery, cable-driven mechanisms remain standard but require high locking forces, causing tendon fatigue and friction. Magnetic actuation eliminates the need for cable transmissions but suffers from low load-bearing capacity and lacks coaxial rotation. We present a magnetic rotary actuator (MAGTWIST) that exploits a traveling wave to achieve a large motion range, stepless rotation, and controllable (un)locking. MAGTWIST features an undulating belt, inspired by peristalsis, and made from a thermo-responsive polymer. Torque generated by an applied magnetic field engages sliders with the undulation, inducing localized deformation that forms a traveling wave around a circular path. Switching between (un)locked states is done by Joule heating. Heating softens the belt within 3.0 s, allowing the wave to travel in a circle arc of up to 270°. Cooling restores stiffness within 5.3 s, halting the wave and achieving stepless shape-locking. Once stiffened, actuation torque rises from 4.5 to 250 N·mm, securing the rotary position and increasing load-bearing capacity. The tubular design with an inner and outer diameter of 4 and 8 mm integrates as an end-effector in a robotic manipulator, as demonstrated through gripping and in situ shape transitions during minimally invasive surgical tasks.

1 | Introduction

Robotic systems are increasingly deployed in hazardous, confined environments that are otherwise inaccessible to humans. Examples include robots for in-space inspection, aeroengine maintenance, search-and-rescue operations, and minimally-invasive surgery [1]. Such robots require joints and actuators that are compact yet dexterous, delivering precise motion under tight geometric constraints and high loads.

In minimally invasive surgery, robot-assisted systems are designed to mimic the skills of a clinician with hand-like dexterity [2, 3]. Replicating a human hand in a robotic system requires, alongside pitch and yaw, a lockable rolling mechanism with 180° range of motion [4]. This functionality is typically achieved using cable drives, which provide precise movements and large forces to the robot. This comes at the expense of cable friction, predefined degrees of freedom (DOFs), and mechanical components like gears and pulleys, which pose challenges for miniaturization [5].

In contrast to cable drives, magnetic actuation systems use external magnetic fields to control magnetic components. The human body is permeable to magnetic fields, making magnetic actuation suitable for medical applications. Magnetic fields can be generated externally to the human body using arrays of electromagnetic coils [6] or permanent magnets [7], and internally using miniature coils embedded within surgical instruments [8,

---

9]. However, the actuation of a magnetic device via magnetic fields is limited to two rotational DOFs, as no torque can be generated around its magnetic moment axis [10].

Magnetic actuation can be combined with selective stiffening and softening of robotic segments to circumvent this 2-DOF limitation. This creates localized resistance to a magnetic field within the robot structure, allowing control of individual DOFs in an otherwise underactuated system [11]. Nonetheless, rigidly fixed magnets constrain the system to predefined DOFs and prevent independent tip rotation. Integrating a lockable rotary mechanism into the magnet would enable dedicated tip rotation and, by reorienting the magnetic moment axis, expand magnetic manipulation options beyond those of fixed magnets.

Rotary mechanisms are often designed using compliant joints [12–14]. They can be fabricated as a monolithic structure, reducing weight, part count, and backlash while enhancing precision [15]. Configured as 1-DOF flexure joints, they have been implemented in tendon-driven laparoscopic and magnetically-actuated neurosurgical instruments [16, 17]. However, the finite bending nature of traditional compliant joints renders them unsuitable for 180° hand-like rotation.

The principle of peristalsis can be an inspiration for overcoming range-of-motion limits in compliant elements. Peristalsis is a transport mechanism within the human body, consisting of coordinated muscle contractions that produce wave-like movements in luminal structures such as the fallopian tubes, small intestine, and esophagus [18–20]. While numerous works have adapted wave-like peristaltic actuation for transportation and locomotion [19, 21–24], few have applied this principle to joint motion or locking. Notably, Qi et al., used an elastic tube to modulate the moving resistance of an inner pneumatically driven piston to achieve a rotary motion [25]. However, onboard fluidic actuators pose significant hurdles to miniaturization. Biomimetic research on peristaltic pumps also led to actuators based on flexible materials like silicone, dielectric elastomers, or magnetic elastomers [26]. For the latter, Chossat and Shea designed a permanently magnetized elastomer rotating actuator using traveling waves [27]. However, this non-miniaturized concept relies on friction for torque transmission, which limits load-bearing capacity and makes the transmitted torque inherently frequency-dependent. Similarly, piezoelectric traveling-wave rotary actuators are highly frequency-dependent and rely on friction coupling. While they provide high positioning accuracy and rapid response, piezoelectric actuation requires high voltages [28–30], which introduces hardware and safety concerns in a surgical environment.

In contrast to friction-based traveling-wave mechanisms, tunable-stiffness elastomers can transmit torque via form-fit by conforming to intricate geometries. Combined with a separate magnetic component, torque can be transmitted magnetically and modulated through the elastomer's stiffness state. Elastomers integrated with low-melting-point alloys (LMPAs) gain tunable stiffness with a high stiffness-change ratio and rapid thermal response, enabling applications in flat, multilayered structures such as sensors, flexible antennas, and robotic grippers [31]. In minimally invasive surgery, LMPAs have been used to design variable stiffness catheters that ensure stability during surgical tasks and flexibility for navigation [32, 33]. However, the discrete melting point of eutectic LMPA makes it difficult to achieve gradual stiffness regulation, and its toxicity poses health risks if not securely encapsulated [31].

Unlike LMPAs, shape memory polymers (SMPs) are biocompatible and offer continuous stiffness regulation. SMP-actuators can be designed to exhibit multiple transition temperatures triggered by external stimuli such as heat, light, electric, or magnetic fields [34, 35]. In addition, SMPs are compatible with 3D printing, enabling the low-cost fabrication of complex geometries [36]. Shape memory alloys (SMAs) present a less cost-friendly alternative to SMPs, offering higher energy density that enables larger stroke lengths. However, SMA-based rotary actuators typically rely on tension wires or torsion springs [37–39], which require intricate wire routing as the heat-induced memory effect scales with wire length.

Here, we present a **MAG**netically-driven rotary actuator using a **T**raveling **W**ave with **I**ntegrated **S**tiffness **T**unability (MAGTWIST). Inspired by peristalsis, MAGTWIST addresses constraints in range of motion and load-bearing capacity, while enabling stepless rotation. An external magnetic field induces a torque on an internal permanent magnet that drives sliders against a variable-stiffness belt, generating a traveling wave. The resistance to wave propagation depends on the elasticity of the belt, which is modulated via Joule heating. In the soft state, torque drives the wave in a peristaltic-like fashion to achieve bidirectional rotation of 270°, exceeding the 180° mobility of the human hand. As a traveling wave does not depend on discrete positions, MAGTWIST can rotate in a stepless manner. Upon cooling, stiffness is restored, halting wave propagation and achieving a shape-lock that withstands high torsional loads for secure positioning. Beyond rotational fixation, the lockable rotation enables intraoperative reprogramming of the magnetic moment. Integrated into a continuum manipulator, MAGTWIST can reorient its magnetic moment, and upon locking, enables in situ shape reconfiguration under external magnetic fields. Concurrently, surgical tools can be deployed through an internal lumen, supporting tasks such as tissue resection, endoscopy, and biopsy.

2 | Design

This section presents the design of MAGTWIST, beginning with the mechanism and operational principle, followed by a finite element analysis of its structural mechanics. The thermal and magnetic actuation strategy is then described, and finally, experiments are conducted to characterize the reaction moment, stall torque, and fatigue limits.

2.1 | Mechanism and Operational Principle

The concept of MAGTWIST is illustrated in Figure 1. Inspired by peristalsis (Figure 1A), the design inverts the usual cause-and-effect relationship: A solid drives the wave to travel (Figure 1B). This principle is embodied in a variable-stiffness belt (VS-belt) featuring a protruding, outward-facing traveling-wave (Figure 1C). It provides stepless rotation and controllable (un)locking using thermal actuation. An integrated permanent

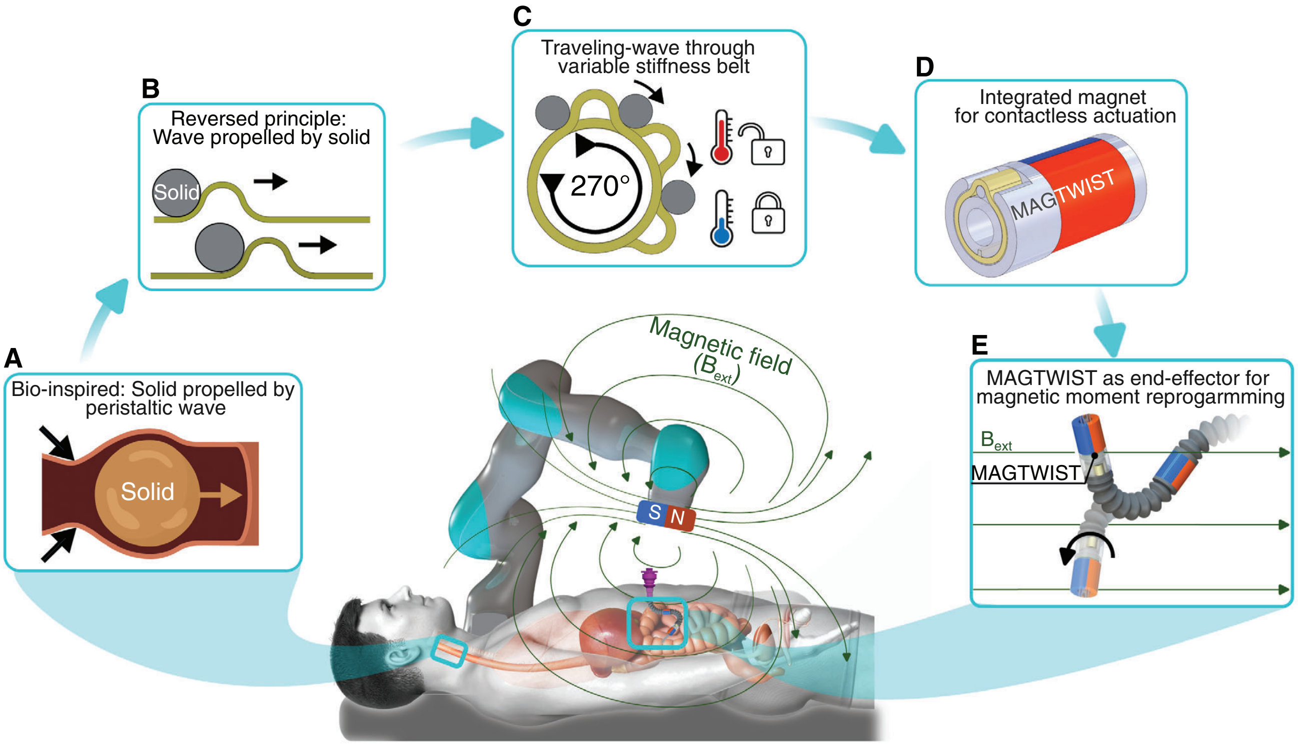

FIGURE 1 | (A) Peristalsis involves wave-like muscle contractions in luminal structures that transport fluids and solids. (B) Reversed principle: a solid object propels the wave, rather than a traveling wave propelling the solid. (C) A rotary mechanism with a variable-stiffness belt for traveling-wave actuation. Joule heating enables (un)locking of the traveling wave, allowing stepless rotations. (D) An external magnetic field induces torque on the permanent magnet to propel the wave. The magnet's dipole lies in the traveling-wave plane. (E) MAGTWIST integrated in a surgical manipulator enables tip rotation and, through reorientation of the magnetic moment, shape change. Human model adapted from Depositphotos (Image ID 386863794), used under Standard License.

magnet experiences torque in the plane of the wave, driving sliders against its contour (Figure 1D). As the magnetic moment of the permanent magnet is linked to the rotation and locking of the traveling wave, torques can be applied to any axis, enabling pose changes when integrated into a continuum manipulator (Figure 1E).

MAGTWIST targets applications in confined workspaces, featuring an inner and outer diameter of 4 and 8 mm, respectively. Integrated with flexible bellows, it forms a compact, magnetically steerable manipulator, as shown in Figure 2A(i–ii) (please refer to Section 3 for details of the manipulator design). MAGTWIST comprises coaxially nested inner and outer shafts with the VS-belt positioned in between (Figure 2A(iii)). The VS-belt is anchored to the inner shaft for torque transmission, while sliders built into the outer shaft partially deform the VS-belt into a wave pattern, as shown in the transverse section view of Figure 2B. As shown in the sagittal cross-section view, a permanent magnet is fixed to the outer shaft (Figure 2C). Under an external magnetic field, the magnet generates torque that drives the sliders against the wave, thereby transmitting torque to the inner shaft. An end cap fixed to the distal end of the inner shaft serves as a mechanical stop, ensuring axial stability of the outer shaft and VS-belt.

At low temperature, the VS-belt remains stiff and its protruding wave transfers torques from the outer shaft to the stationary inner shaft, thereby locking the outer shaft's rotation. At elevated temperature, the VS-belt becomes deformable, and the outer shaft drives the traveling wave around the circumference. In this state, the outer shaft is unlocked and can rotate around the stationary inner shaft. Once the temperature drops, the VS-belt regains stiffness, and the wave maintains its position against the sliders through shape-lock.

The VS-belt consists of two layers of thermoresponsive polymer encapsulating a heater element (Figure 2D). The heater is laser-cut from a stainless steel foil and placed between the two layers of polylactic acid (PLA) printed by fused deposition modeling (FDM). Heat pressing is used to bond the layers together, after which the assembly is formed into a belt shape (please refer to section 5 for manufacturing details).

2.2 | Numerical Analysis of Structural Mechanics

Numerical analysis is used to guide the design of MAGTWIST, study its structural behavior during rotation, and the effect of altered design parameters on its reaction moment characteristic. This allows motion prediction under given loads and the adaptation for designs for scenarios that require specific actuation torques or operate within limited magnetic field strengths. MAGTWIST is actuated by overcoming the deformation resistance of the VS-belt under imposed rotation and the

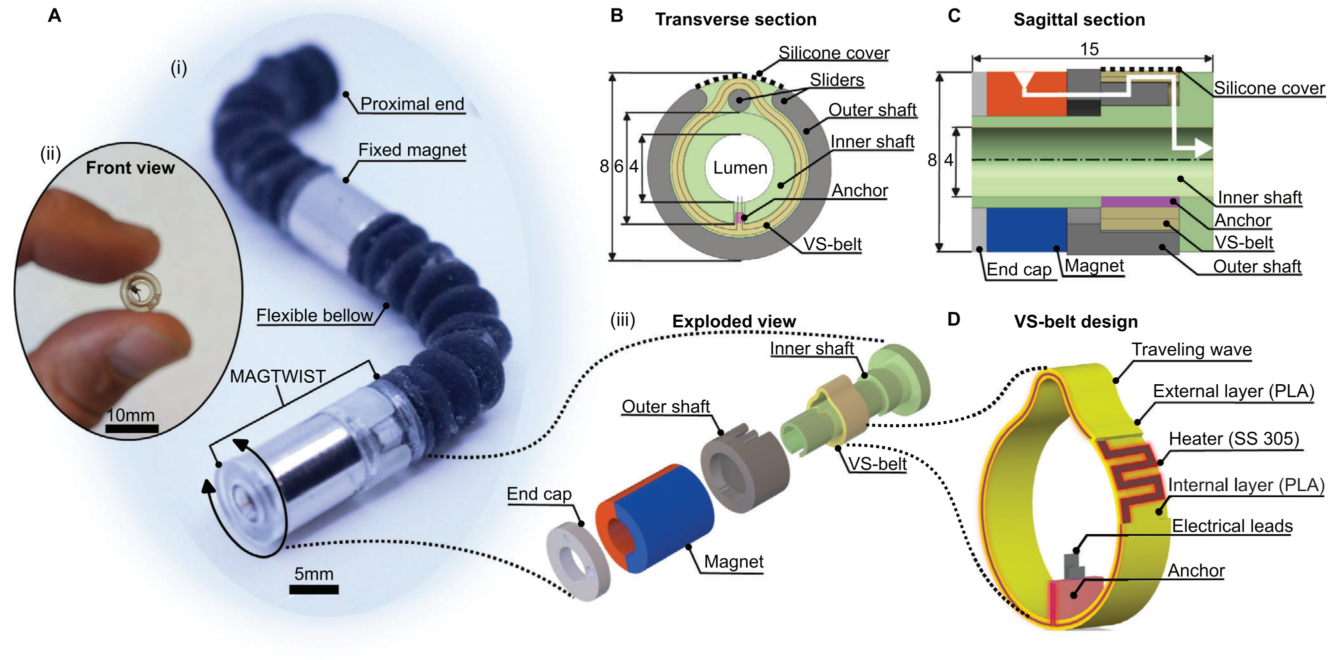

FIGURE 2 | (A) (i) MAGTWIST connected to flexible bellows forming a manipulator, (ii) Front view of MAGTWIST to scale, (iii) MAGTWIST assembly in exploded view (B) Transverse cross-section view: Sliding elements enclose the undulation and transmit torque. (C) Sagittal cross-section view: Torque induced on the magnet is transmitted from the outer to the inner shaft via the VS-belt (white line indicates torque-transmission path). (D) Variable-stiffness belt consists of a heating element embedded between internal and external layers of thermoresponsive polymer. All units are in mm.

friction between adjacent components, both of which manifest as the reaction moment (M_R). The actuation frequencies in experiments are low ($\leqslant$ 1 Hz). Consequently, a quasi-static approximation (without inertial effects) is assumed to be adequate for capturing primary trends of interest, such as wave-propagation behaviour and reaction moment profile. M_R is studied via quasi-static finite element model in COMSOL Multiphysics 6.0, using a hyperelastic material feature with temperature-dependent experimental data to model nonlinear softening effects of the VS-belt. Sliding-contact is modelled using a static Coulomb model within a quasi-static equilibrium sequence.

M_R is directly influenced by design parameters, including the slider diameter (D_{Slider}), the angle between sliders (β), VS-belt thickness (t_{belt}), friction coefficient (μ), and operating temperature (T) (Figure 3A (i)). To assess the influence of each parameter on M_R, we conduct a one-factor-at-a-time sweep in which each design parameter is varied independently, and taking peak M_R over the rotation angle (θ) in the soft state as the outcome. Next to the design parameters, there are also state-dependent parameters such as the strain of the VS-belt (ϵ_{belt}), the gap between the VS-belt and the central slider (d_{gap}), and the contact angle between slider and VS-belt (ϕ_{belt}) (Figure 3A (i)). These parameters vary during rotation and passively influence (M_R). Fabrication and actuation constraints impose bounds of 0.6 mm for the VS-belt thickness, 1.5 mm for the slider diameter, and 5 N·mm for the actuation torque. These values serve as baseline constants in the subsequent analysis, except when they are themselves the parameter under investigation.

2.2.1 | Design parameter effects

Increasing β from 50° to 80° increases the distance between the sliders, which reduces ϕ_{belt}. Consequently, the VS-belt bends less sharply as it propagates, reducing M_R from 5 to 2 N·mm (Figure 3B). Therefore, β of MAGTWIST is set to 55° to meet the actuation torque requirement of less than 5 N·mm. In contrast, increasing D_{Slider} from 1.1 to 1.6 mm results in a greater ϕ_{belt}, causing M_R to rise from 2 to 5 N·mm (Figure 3B). As t_{belt} increases from 0.2 to 1.0 mm, M_R rises from 2 to 18 N·mm as a result of the increased stiffness of the VS-belt (Figure 3C). Raising the operating temperature from 20°C to 80°C decreases M_R from 203 to 4.2 N·mm as the VS-belt material becomes soft at higher temperatures, thereby enabling continuous stiffness regulation (Figure 3D). The friction coefficient substantially affects M_R due to contact between the VS-belt and the inner and outer shaft, with the peak of M_R increasing from 2 to 11 N·mm as μ rises from 0.5 to 0.8 (Figure 3E).

2.2.2 | State-dependent parameter effects

During $\theta \in [0°, 270°]$, the VS-belt elongates due to the tangential tension exerted by the slider. As a result, ϵ_{belt} increases notably beyond 160°, experiencing a total strain of 2.1% (Figure 3F). This effect is accompanied by the increase of d_{gap} up to 0.5 mm ($d_{\text{gap}^{\max}}$) (see Figure 3A(ii), G, and Video S1). Additionally, the stress distribution (σ_{vM}) within the VS-belt during rotation and the contact pressures (p_c) at its interfaces with

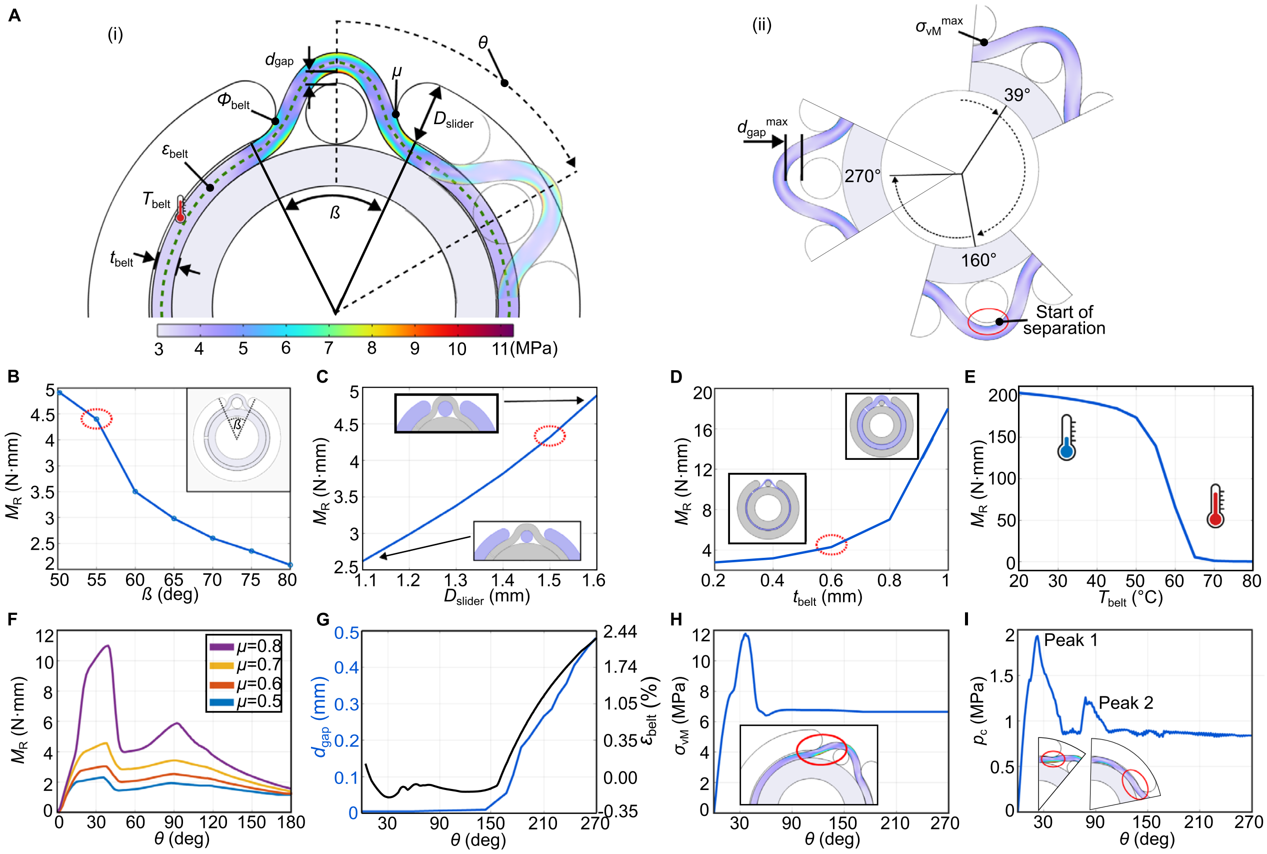

FIGURE 3 | (A) (i-ii) Design parameters for MAGTWIST and their effects on system performance under simulation: (B) Slider angle (β) as a function of reaction moment (M_R). (C) Slider diameter (D_{Slider}) as a function of M_R. (D) Variable-stiffness belt (VS-belt) thickness (t_{belt}) as a function of M_R. (E) VS belt temperature (T) as a function of M_R. (F) Friction coefficients (μ) as a function of M_R. (G) VS belt strain (ϵ_{belt}) and undulation gap (d_{gap}) as a function of rotation angle (θ). (H) Von Mises stress (σ_{vM}) within VS-belt as a function of θ. (I) Contact pressure (p_c) as a function of θ. (B–D) Values applicable to MAGWIST are labeled with red dashed circles.

adjacent components are studied. When MAGTWIST reaches a rotation angle of $\approx$39°, a peak stress (σ_{vMmax}) of 12 MPa is observed within the VS-belt (Figure 3H). The stress, σ_{vM}, subsequently levels off at 6.5 MPa and remains well below the 53 MPa yield strength of the PLA material used. Two dominant peaks in p_c occur between the VS-belt and adjacent sliders: one at 23° with a magnitude of 1.9 MPa, and another at 78° reaching 1.25 MPa. Beyond the second peak, p_c stabilizes near 0.9 MPa (Figure 3I). This analysis provides quantitative design guidelines for torque control and reveals structural behavior that indicates potential load limits and fatigue mechanisms.

2.3 | Thermal Management

Beyond the mechanical performance, effective thermal management is essential for regulating the stiffness of MAGTWIST. The PLA used to fabricate the VS-belt is thermomechanically analyzed, followed by a thermal characterization of the VS-belt itself.

The storage modulus (E') represents the elastic, energy-storing component, while the loss modulus (E'') quantifies the viscous, energy-dissipating response. For PLA, E' is temperature-dependent, as the dynamic mechanical analysis across $T_{PLA} \in [0, 80]$ °C shows a significant drop in E' as temperature rises (Figure 4A). The drop occurs around the glass transition temperature ($T_g \approx 65°$C), which is identified by the peak of $\tan\delta = E''/E'$. At $T_{stiff} = 55°$C, PLA exhibits a storage modulus of $E'_{stiff} \approx 2.7$ GPa, with E' increasing further at lower temperatures. As the temperature rises to $T_{soft} = 80°$C, PLA transitions into a soft state with $E'_{soft} \approx 10$ MPa.

Building on these material characteristics, the effective operation of MAGTWIST depends on the thermal response of the VS-belt under different actuation currents. Short heating times are achieved with higher currents: in air at room temperature (T_{air} = 20°C), the VS-belt is heated from T_{stiff} to T_{soft} within 3 s at 1.0 A, followed by passive cooling back to T_{stiff} in an average of 5.3 s (Figure 4B). Reducing the current to 0.7 A increases the heating duration by 10 s. By applying a relatively low current of 0.35 A, the VS-belt gradually transitions from T_{stiff} to T_{soft} in 84 s (Figure 4C). In this case, passive cooling is prolonged to 18.2 s due to heat accumulation in adjacent components. Currents of 0.25 A and lower are insufficient to reach T_{soft}. These results demonstrate that MAGTWIST can reliably and reversibly switch between stiff and soft states within seconds, a capability essential for rapid adaptation to surgical scenarios.

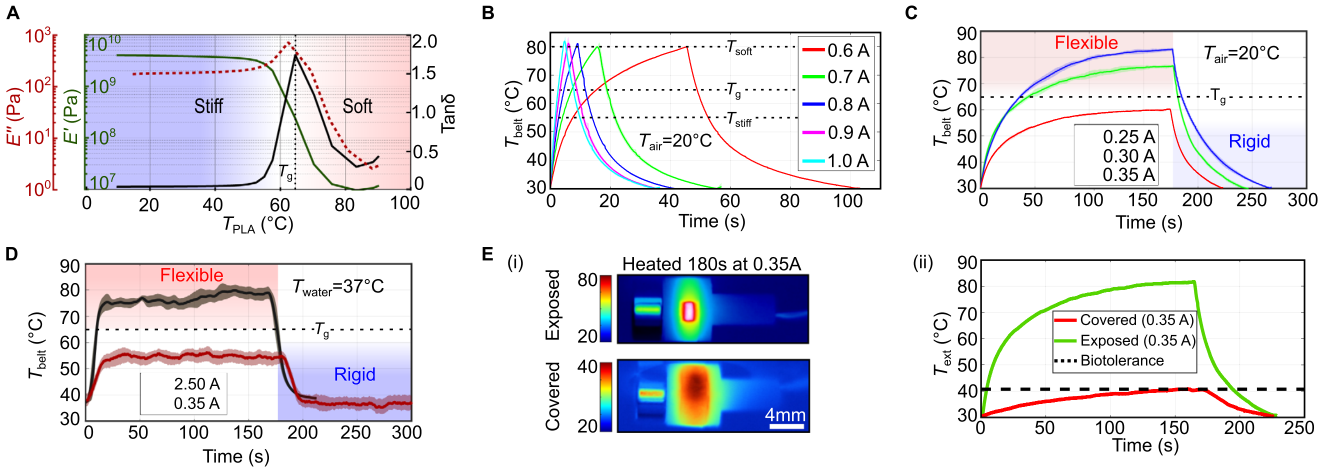

FIGURE 4 | (A) Identification of the glass transition temperature (T_g) of the variable stiffness material. (B) Heating time at high currents and (C) at low currents. (D) Thermal response of the Variable-stiffness belt submersed in water. (E) (i) Thermal images after gradual heating, (ii) Thermal profile with exposed surface versus covered through silicone. In (B)–(D), the mean of three measurements is presented, with light backgrounds indicating ± standard deviation.

The VS-belt's thermal performance under high heat dissipation conditions was assessed in water at a physiologically relevant temperature ($T_{water} = 37°C$) without forced flow (Figure 4D). The results indicate that a minimum current of 2.5 A is required to reach the actuation temperature of 80°C, reflecting the medium's strong heat sinking due to convection and heat capacity. In contrast, only 0.35 A is needed in air (Figure 4D). Consequently, the VS-belt requires 5.9 s to stiffen in water, which is comparable to the 5.3 s it takes in air, despite the water being at 37°C.

For safe operation within the human body, the surface temperature of a surgical instrument must remain below 41°C [40]. During the transition from the stiff to the soft state, the maximum external surface temperature (T_{ext}) of MAGTWIST reaches 80°C with an exposed VS-belt but is reduced to 40°C when covered with silicone (Figure 4E(i)). This remains below the biotolerance threshold, minimizing the risk of thermal damage to human tissue (Figure 4E(ii)).

2.4 | Magnetic Actuation

Magnetic actuation systems typically use arrays of electromagnetic coils [41,42] or robot-mounted magnets [7] to generate the magnetic field to control a permanent magnet. The MAGWIST is equipped with a permanent magnet at its distal tip, such that magnetic torques can control its orientation.

Electromagnets arranged in a Helmholtz configuration generate a highly uniform magnetic field. In such a field, a magnet experiences a magnetic torque ($\boldsymbol{\tau}_m \in \mathbb{R}^3$) that tends to align its magnetic moment ($\mathbf{m} \in \mathbb{R}^3$) with the applied field ($\mathbf{B} \in \mathbb{R}^3$). The magnetic torque is given by

$$\boldsymbol{\tau}_m = \mathbf{m} \times \mathbf{B}. \tag{1}$$

The torque reaches its maximum when **m** and **B** are perpendicular, and it is zero when they are aligned. For MAGTWIST, $\boldsymbol{\tau}_m$ must overcome both the deformation resistance of the VS-belt and the friction between adjacent components. This can be achieved by increasing either the applied field **B** or the magnetic moment **m** of the permanent magnet, which is expressed as

$$\mathbf{m} = \frac{\mathbf{B}_r V}{\mu_0}, \tag{2}$$

where $\mathbf{B}_r$ is the residual magnetic flux density, V the magnet volume, and μ_0 the permeability of free space.

As described by Equation (1), a magnetic moment cannot be rotated about its magnetization axis, restricting magnetic manipulation to two rotational DOFs [43]. This limitation is evident in magnetically-driven manipulators with rigidly fixed magnets, as they become unresponsive once **m** aligns with **B** [32,33,44,45]. In contrast, MAGTWIST provides a manipulator with bidirectional 270° tip rotation, allowing the two magnetically accessible DOFs to be reoriented. This enables sequential access to any desired rotation axis without imposing stress on the manipulator or surrounding structures.

2.5 | Design Validation

This section experimentally validates the torque response and controllable locking function of MAGTWIST within a Helmholtz coil setup that generates magnetic torque. The resulting reaction moment (M_R) is measured using a torque sensor (Figure 5A(i)). Two actuation modes are applied in the experiments: dynamic actuation with rotating fields of 15 mT amplitude at 0.8 Hz, and static actuation with a linearly ramped magnetic field increasing from 0 to 40 mT over 10 s (Figure 5A(ii)). While the dynamic field produces continuous torque throughout the rotation cycle, the static field applies a gradually increasing torque until a snap-through event occurs.

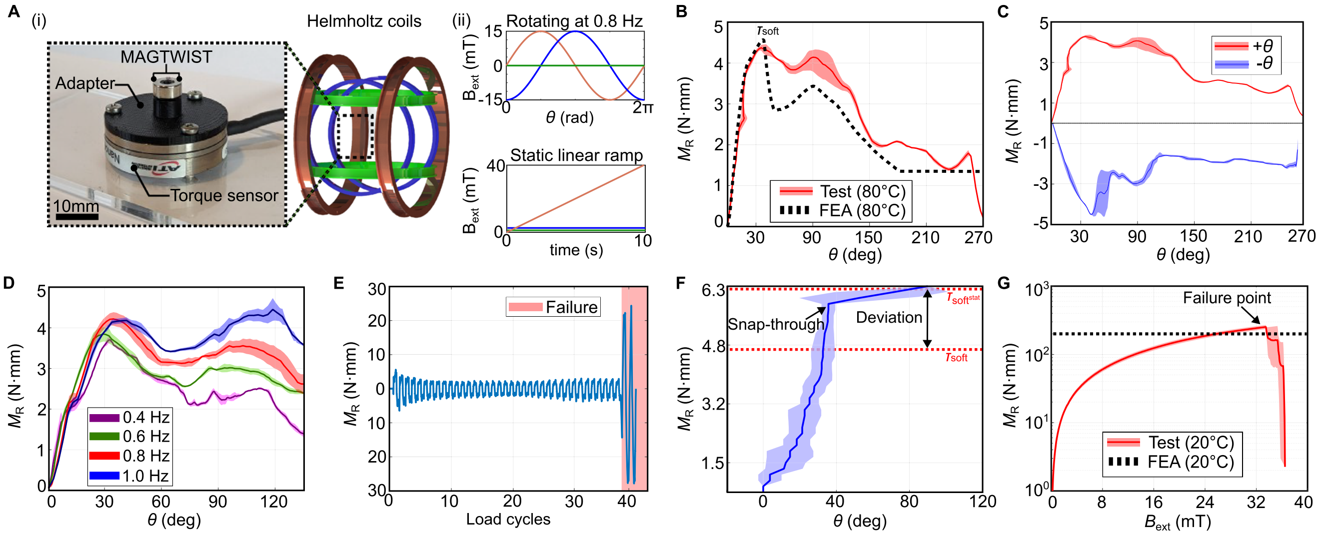

FIGURE 5 | (A) (i) Experiment setup with Helmholtz coil and torque sensor, (ii) Using rotating and ramped static magnetic fields. Rotating field experiments: (B) Mean reaction moment (M_R) over 0°–270° comparing experiment and FEA. (C) Bidirectional measurements. (D) Reaction moment across different actuation frequencies. (E) Cyclical fatigue loading of the variable-stiffness belt. (F,G) Static ramped field experiments: (F) Soft-state actuation under a ramped field. (G) Stall torque in the stiff state. In (B, C, D, F, G), the mean is shown with shaded regions indicating standard deviation; panel (E) shows a representative trial.

2.5.1 | Dynamic field actuation

Figure 5B shows M_R over $\theta \in [0^\circ, 270^\circ]$, in close agreement with the results of the finite element analysis (FEA). Maximum peaks of 4.2 N·mm (experiment) and 4.5 N·mm (FEA) are observed, denoted as τ_{soft}, which represents the torque required for rotation at T_{soft}. Figure 5C further shows M_R measured bidirectionally under rotating fields, with a peak deviation of 0.35 N·mm between clockwise and counter-clockwise rotation. In Figure 5D, the effect of actuation frequency (0.4–1.0 Hz) is measured over $\theta \in [0^\circ, 140^\circ]$ with the per-frequency mean ±SD shown. At each frequency, two reproducible peaks can be observed. Averaged across frequencies, the first and second peaks are 4.12 (±0.20) N·mm and 3.31 (±0.79) N·mm, respectively.

Figure 5E shows a fatigue test with MAGTWIST undergoing repeated load cycles of $\theta \in [0^\circ, 270^\circ, 0^\circ]$ at 1 Hz. As outlined in Section 2.2, both strain (ϵ_{belt}) and gap distance (d_{gap}) increase over $\theta \in [0^\circ, 270^\circ]$ due to slider-induced stretching. As a result, the less constrained VS-belt is more prone to buckling and undergoes greater deformation as cycling continues. In addition, PLA exhibits time-dependent viscoelastic behaviour. Therefore, repeated load cycles may introduce localized plastic deformation within the VS-belt material, potentially accelerating material fatigue. This combination leads to traveling-wave instability and failure after 38 cycles, with actuation frequencies >1 Hz expected to further decrease the load cycles of FDM-printed PLA specimens due to mechanical fatigue and self-heating [46]. Load-cycle life could be improved by reducing local strain through optimized undulation geometry, tighter tolerances, different polymer, supports to maintain slider–belt contact, and adopting rolling elements to reduce friction.

These results confirm the accuracy of the simulation-based M_R profile, highlighting frequency- and direction-dependent actuation characteristics, as well as fatigue limits and potential fatigue life improvements. Additionally, Figure S1 shows a detailed view of the alignment and mechanical interactions of the MAGTWIST components in the simulated model and physical prototype.

2.5.2 | Static field actuation

Actuating MAGTWIST with static fields offers an alternative mode of operation when rotational fields are impractical due to system constraints. However, static fields induce only 90° of rotation per field direction; further rotation requires reorienting the applied field. Under those conditions, at T_{soft}, MAGTWIST gradually aligns with the static field until it abruptly snaps at $\approx 39^\circ$ into full 90° alignment (Figure 5F). The snap-through occurs at a torque of 6.3 N·mm, denoted as τ_{softstat}. Compared to τ_{soft}, this is higher by 1.8 N·mm due to static friction: torque rises until the maximum static friction is reached, after which it abruptly drops to the lower kinetic friction. In addition, the magnetic torque decreases gradually over $\theta \in [0^\circ, 39^\circ]$ as the magnetic moment moves away from perpendicular to the static field (see Equation (1)).

The maximum stall torque is determined using a magnet with a dipole moment of 8 A·m^2. Across three trials at 20°C, MAGTWIST withstands an average stall torque of 250 N·mm before the anchor of the VS-belt fractures. Compared to the torque required for rotation in the soft state ($\tau_{\mathrm{soft}} \approx 4.5$ N·mm), the measured stall torque of 250 N·mm represents a ≈ 56-fold increase in stiffness, and exceeds the peak reaction moment of 203 N·mm predicted by FEA (Figure 5G). These results demonstrate a controlled switch between a low-torque state for MAGTWIST rotation and a high-torque state for secured positioning, an essential capability when used as a surgical end-effector.

3 | Demonstrations

This section highlights the key advantages of MAGTWIST through three demonstrations: The first demonstrates an extensive range of motion through sequential obstacle navigation using stepless rotation. The second demonstrates magnetic moment reorientation with locking capability through distinct shape reconfigurations. The third combines tip rotation with shape transitions while utilizing the internal instrument channel, as shown in a simulated tissue resection. In each experiment, MAGTWIST is mounted on a continuum manipulator that combines low flexural rigidity to allow bending, with high torsional rigidity to reduce undesired torsional effects. Two continuum sections are constructed from convoluted bellow tubes, reinforced with a double-helix structure to enhance torsional rigidity. The manipulator is divided into two segments. The distal segment comprises MAGTWIST, which (un)locks the rotation of the tip magnet, while the proximal magnet is fixed. The manipulator features an internal lumen for power supply and accessory deployment.

3.1 | Sequential Tip Rotation

This experiment demonstrates how MAGTWIST utilizes its wide rotation range on a manipulator to precisely control and guide an object through a series of obstacles.

MAGTWIST is mounted on a robotic arm, with a manually rotatable external permanent magnet positioned beneath it (Figure 6A). Five acrylic plates, each with identical cut-outs, are stacked with 8 mm gaps between them and rotated by 45° relative to each other to form an obstacle maze (Figure 6B (i)). A customized 3D-printed compliant gripper (3.8 mm diameter) is pre-inserted through the instrument channel to grasp a 50 mm long foam beam and guide it through the obstacle maze (Figure 6B (ii)). The gripper is engaged and released by manually actuating a handle.

In Figure 6C, the beam is initially positioned horizontally, at a 45° angle to the first cut-out (Figure 6C (i)). To align with the first cut-out, MAGTWIST is rotated 45° around the z-axis, after which the gripped beam is lowered and guided through the first plate (Figure 6C (ii)). The 45° rotation and lowering are then repeated while guiding the beam through each of the plates in sequence (Figure 6C (iii–iv)). After guiding the beam through all five cut-outs, the experiment is concluded by dropping the beam at the 270° orientation by releasing the gripper (Figure 6C (iv)). See Video S2 for a complete demonstration. This demonstration is performed with an average completion time of 135 s ± 18 s with successful placement of the beam in 2 out of 3 trials.

Permanent magnets generate non-uniform fields with strong gradients, making the shape reconfiguration of MAGTWIST challenging. Small changes in position and improper alignment of the permanent magnet may induce spatially varying torques along the manipulator, leading to unstable control. When properly aligned, however, forces generated by field gradients are small relative to the applied torque and do not impair rotational actuation. When actuated manually using an external permanent magnet with a magnetic dipole moment of 230 $\text{A}\cdot\text{m}^2$, a minimum reliably controllable angular displacement from rest of 2° ± 0.5° is achieved at a 130 mm distance (see Figure S2).

3.2 | Shape Reconfiguration

Previous work on magnetic continuum manipulators with variable stiffness segments have been developed to achieve selective bending [33, 44, 47, 48], or a combination of selective bending and apical expansion [49,50]. Implementing multiple fixed magnets along a manipulator's length enables selective control of individual DOFs without variable stiffness segments, but relies on highly localized magnetic fields, which increases system complexity [43]. In contrast, fixed but oppositely magnetized magnets can be employed to achieve S-, C-, and J-configurations under a uniform, non-localized magnetic field [51]. However, a permanently fixed misalignment between magnets constrains a manipulator's deformation to 2D, planar shapes.

MAGTWIST can overcome this bottleneck by rotating and locking the distal magnet of a two-sectioned continuum manipulator. Consequently, the manipulator can transition successively between 2D and 3D shapes under a uniform, non-localized magnetic field (Figure 7A). When the magnetization of MAGTWIST and the proximal magnet are aligned in the absence of a magnetic field, no torque is generated, and the manipulator remains in an I-shape (Figure 7A(i)). Under a magnetic field of 20 mT, both segments deflect in the same direction, and the manipulator adopts a C-shape (Figure 7A(ii)). Rotating MAGTWIST by 180° creates a 180° misalignment between the magnetization of MAGTWIST and the proximal magnet. Consequently, under a magnetic field of 20 mT, the corresponding segments deflect in opposite directions, causing the manipulator to adopt an S-shape (Figure 7A(iii)). At 90° misalignment, MAGTWIST undergoes out-of-plane bending, and the manipulator adopts an S-shape in 3D (Figure 7A(iv)). When the distal MAGTWIST is more exposed to the magnetic field, it experiences a greater torque than the proximal magnet, and the manipulator adopts a J-shape (Figure 7A(v)) (see Video S3 for a complete demonstration). This demonstration is performed three times with an average completion time of 118 s ± 20 s.

Shape reconfigurations are achieved by rotating MAGTWIST under 20 mT in the soft state and by deflecting it under 30 mT in the stiff state (Figure 7B). This approach uses a Helmholtz coil to generate highly uniform fields, achieving a minimum controllable angular displacement from rest of 6° ± 1° (see Figure S2), with stopping possible at virtually any angle. Increasing the field strength can further improve resolution, as smaller angular misalignments then suffice to generate the required torque. Notably, the distal MAGTWIST at the tip must rotate relative to its proximal fixed counter-magnet. This rotation must overcome both the restoring torque arising from their magnetic interaction and the intrinsic actuation torque of MAGTWIST (τ_{soft}). A setup is designed to measure the maximum restoring torque as a function of magnet spacing. This is achieved by mounting the two magnets at right angles: one on a linear slide and the other on a torque sensor (Figure 7C(i)). The experimental results are in good agreement with the magnetostatic FEA, showing that the restoring torque decays exponentially as the

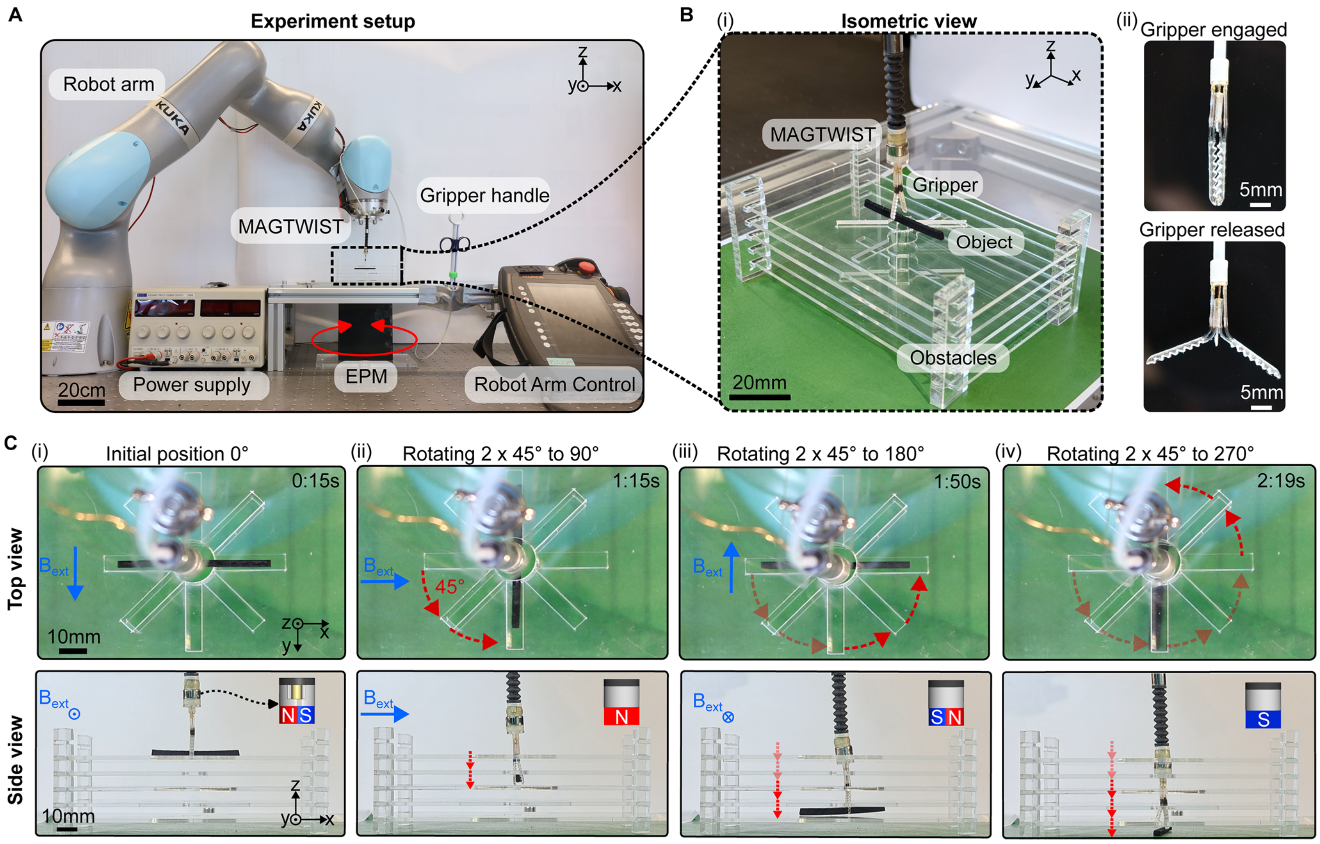

FIGURE 6 | Demonstration of MAGTWIST precisely guiding an object through an obstacle maze. (A) The device is mounted on a KUKA robot arm for vertical motion, with a rotatable external permanent magnet (EPM) beneath providing magnetic torque. (B) (i) Five acrylic plates, each with identical cut-outs rotated by 45° relative to the one below, form the maze, (ii) a 3D-printed compliant gripper, inserted through the instrument channel and actuated manually via a handle, grasps a foam beam and guides it through the maze. (C) (i) Selected frames illustrate the process, with the beam initially positioned horizontally at 45° to the first cut-out, (ii) MAGTWIST is rotated by 45° to align the beam with the first cut-out and then lowered past the first obstacle layer, a sequence repeated for the second layer, (iii) the same rotation–lowering sequence continues through the third, fourth, and fifth cut-outs, (iv) finally, the beam is placed on the ground, having been rotated step-wise through 270°. Please refer to Video S3 for a complete demonstration.

magnet spacing increases (Figure 7C(ii, iii)). With the design at hand, a 30 mm magnet spacing yields a restoring torque of 0.5 N·mm, which must be accounted for when actuating MAGTWIST to achieve shape transitions in the two-section manipulator.

3.3 | Simulated Tissue Removal under Magnetic Guidance

Uterine fibroids, also known as myomas, are the most common benign tumours in women of reproductive age. They can cause abnormal uterine bleeding, bowel dysfunction, and dyspareunia [52]. Myomas are typically removed laparoscopically, called myomectomy. When performed robotically, this procedure is associated with significantly fewer complications [53]. During a laparoscopic myomectomy, large, dense fibrous myomas can restrict the effectiveness of forceps. In such cases, the myomas are removed using corkscrew myoma fixation devices, which vary in thread design and pitch [54]. However, these instruments lack an instrument channel, necessitating additional incisions for tools such as a camera [55], thereby increasing patient risks.

To simulate a robotic-assisted myomectomy on fibrous tissue using MAGTWIST, a custom-made myoma screw (8 mm diameter) is mounted at the tip. A camera (0.9 mm diameter) and a biopsy tool (2.3 mm diameter) are inserted through the 4 mm lumen. A silicone model simulates a contorted organ structure, while blueberries (target A and B) serve as stand-ins for uterine fibroids (Figure 8A). The procedure is recorded from a top-down perspective, with the oval inset showing the camera's internal view. The experiment is conducted inside a Helmholtz coil setup to generate homogeneous magnetic fields for actuation.

The manipulator is introduced into the workspace from below via a linear slide (Figure 8A). A static external field ($B_{ext} = 10$ mT) is applied to induce a C-shape in the manipulator to reach target A. Once target A is reached, the biopsy tool is deployed to collect a sample (Figure 8B). MAGTWIST is then heated to 80°C, and a rotational magnetic field ($B_{ext} = 20$ mT) is applied to reorient its magnetic moment (m_1) by 180° relative to that of the fixed magnet (m_2) (Figure 8C). Due to opposite dipole directions of m_1 and m_2, a subsequent static magnetic field ($B_{ext} = 20$ mT) induces an S-shape in the cooled-down manipulator to reach target B (Figure 8D). A 270° MAGTWIST rotation is then used to create the screw's drilling motion into target B (Figure 8D). Once the

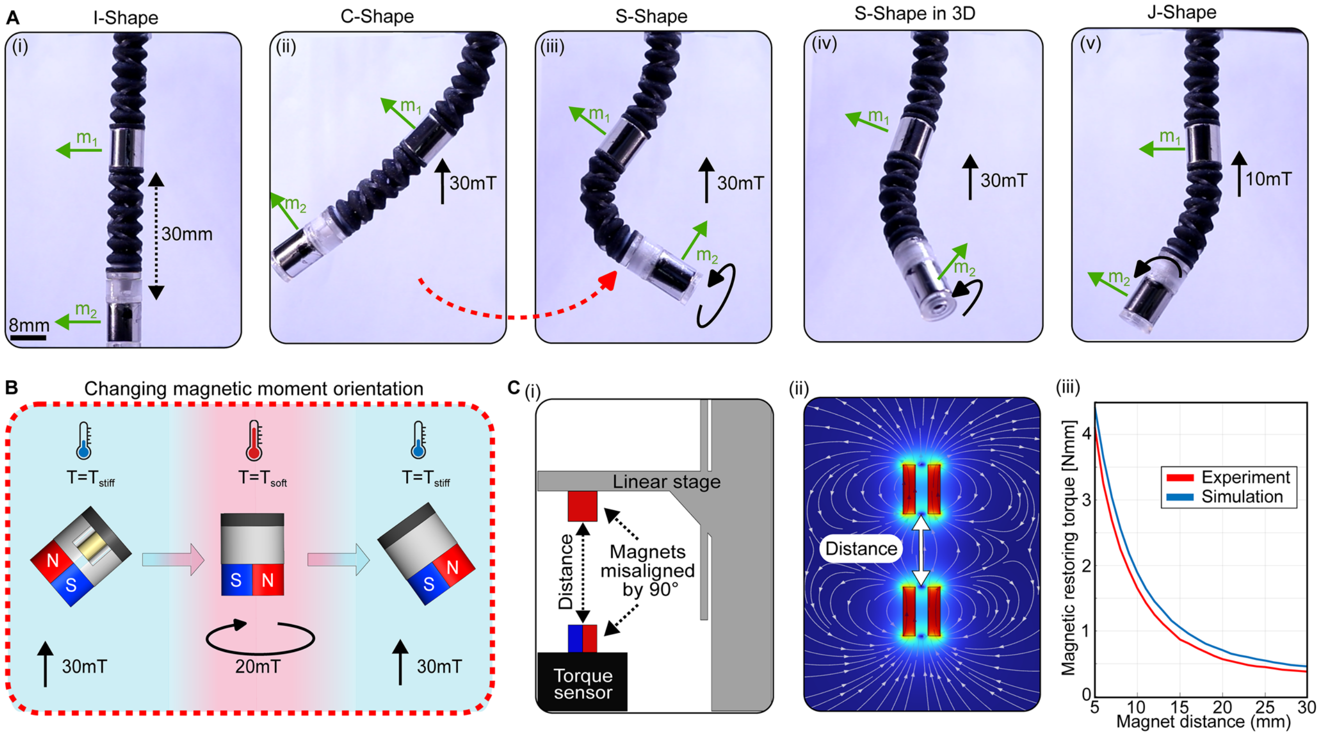

FIGURE 7 | MAGTWIST rotation can be utilized for shape transformations in the stiff state: (A), (i) I-shape (no deflection), (ii) C-shape (magnetic dipoles aligned), (iii) S-shape (magnetic dipoles misaligned by 180°), (iv) 3D S-shape (magnetic dipoles misaligned by 90°), and (v) J-shape (distal torque amplification). Please refer to Video S2 for a complete demonstration. (B) Shape transformations are achieved by changing the magnetic moment of MAGTWIST. (C), (i–iii) Experiment and simulation show the magnetic restoring torque decays exponentially with magnet spacing, reaching 0.5 N·mm at 30 mm distance.

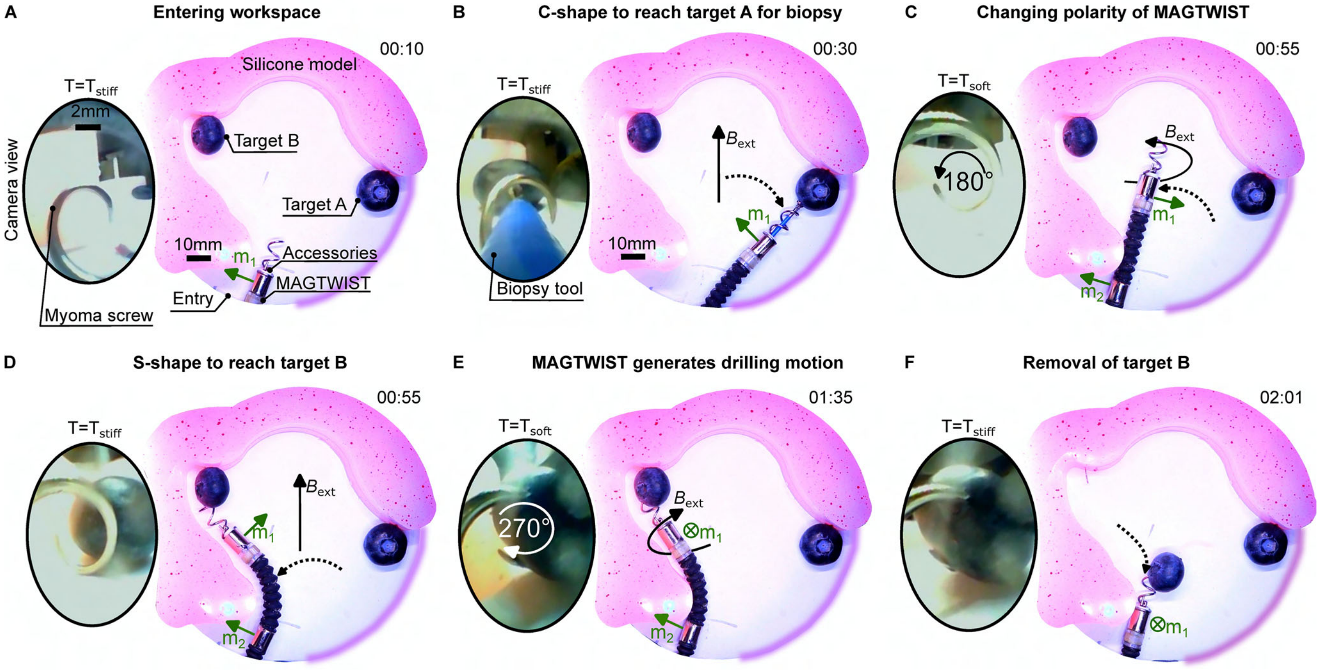

FIGURE 8 | Simulation of robotic-assisted myomectomy using MAGTWIST. (A) Experimental setup with silicone model to replicate organ structure, blueberries as targets A and B, and internal camera view. (B) C-shape induced by static field (B_{ext} = 10 mT) to reach target A and deploy biopsy tool. (C) Heating to 80°C and application of rotational field (B_{ext} = 20 mT) to reorient the magnetic moment (m_1 vs. m_2). (D) S-shape induced by static field (B_{ext} = 20 mT) to reach target B. (E) 270° MAGTWIST rotation to drill with myoma screw into target B. (F) Removal of target B through the entry point. Please refer to Video S4 for a complete demonstration.

TABLE 1 | Overview of the specifications of MAGTWIST.

Specification	Value
Outer diameter	8 [mm]
Inner diameter	4 [mm]
Length	15 [mm]
Weight	5 [g]
Maximum range of motion	270 [°]
Variabel-stiffenss belt thickness	0.6 [mm]
Slider diameter	1.5 [mm]
Slider angle	55 [°]
Rotation torque in soft state	4.5 [N·mm]
Maximum stall torque in stiff state	250 [N·mm]
Minimum heating time	3 [s]
Minimum cooling time	5.3 [s]
Operating temperature	80 [°C]
Maximum Power	50 [W]
Electrical Resistance	8 [Ω]

screw is lodged securely within the target, the manipulator is retracted, thereby removing target B and successfully simulating a myomectomy (see Supplementary Video S4 for complete demonstration). This demonstration is performed five times with an average completion time of 126 s ± 12 s with successful retrieval of target B in 3 out of 5 trials. It showcases that MAGTWIST can rapidly switch between locked and unlocked states, enabling both shape changes for surgical site access and rotation-specific tasks.

4 | Discussion

This work presents MAGTWIST—a novel rotary actuator, inspired by peristalsis. An overview of its specifications is provided in Table 1, while Table S1 places MAGTWIST within the broader context of existing actuation technologies, providing a benchmark across different performance attributes. The key innovation of MAGTWIST is the bidirectional rotation range of 270°, exceeding the 180° mobility of the human hand. The working principle is based on a traveling wave with shape (un)locking enabled by a tunable-stiffness polymer, allowing high load-bearing capacity.

Previous studies have shown magnetically-actuated 2-DOF wristed end-effectors for neurosurgical and gastrointestinal resection tasks [11,56], as well as magnetic catheters for cardiac ablation and endoscopy [33,44]. Yet, none offer distinct end-effector rotation. Our novel traveling-wave concept is therefore the first to introduce controllable and lockable tip rotation to magnetically-actuated surgical instruments.

The load-bearing capacity of MAGTWIST primarily arises from the traveling wave's resistance to propagation, quantified by the reaction moment (M_R) between inner and outer shafts. To analyze M_R during wave propagation, FEA is used and validated through experimental testing. M_R rises markedly from 4.5 N·mm (4.2 N·mm FEA) in the soft state to 250 N·mm (203 N·mm FEA) in the stiff state, a 56-fold (48-fold FEA) increase. Additionally, the FEA highlights that M_R is readily tunable through small geometric edits, e.g., varying the VS-belt thickness from 0.2 to 1.0 mm, which spans nearly an order-of-magnitude change in soft-state M_R, without significantly exceeding the overall architecture. Moreover, continuous temperature variation of the VS-belt enables continuous regulation of M_R, allowing task-specific load-bearing capacity.

The stiffness of the thermo-responsive VS-belt is tuned via Joule heating. At room temperature in air, the heating response time is 3 s at 1 A, and the cooling response time is 5.3 s. Owing to its large surface-to-volume ratio, the VS-belt achieves a cooling rate comparable to an active cooling strategy reported at 4.4 s [44]. An active cooling system could be implemented to achieve cooling in under 5.3 s.

Notably, heating behavior may differ in real biological environments, where tissue thermal conductivity, water content, and perfusion rates influence heat dissipation. Although preliminary results indicate constant heating characteristics in both air and water, tissue heterogeneity and perfusion in vivo may reduce heating and cooling efficiency, highlighting the need for real-time temperature monitoring. The VS-belt is coated with silicone to insulate its exterior to protect surrounding structures from heat. However, an encapsulation failure would expose tissue to temperatures near 80°C, and could cause immediate thermal injury. In addition, excessive leakage current poses a risk of electric shock. Therefore, clinical implementation of MAGTWIST must comply with the IEC 60601-1 standards, which require the leak current on the order of milli-to micro-ampere to prevent electric shock, as well as safeguards against mechanical and thermal hazards for robotically assisted surgical equipment [57].

Our proposed method of using a traveling-wave enables a 4 mm inner lumen with an 8 mm outer diameter, compatible with most commonly used trocars [58], easing the integration into established clinical workflows. Moreover, 8 mm robot-assisted laparoscopic instruments have been shown to significantly outperform 5 mm instruments in tasks such as peg transfer, circle cutting, and intracorporeal suturing [59]. Nevertheless, load-bearing components such as the inner and outer shafts are currently 3D-printed. Manufacturing these parts from biocompatible metals such as titanium would permit further miniaturization, potentially expanding MAGTWIST's applicability to endovascular procedures.

The VS-belt retains advantages of a compliant element, such as eliminating the need for electro-mechanical components, simplifying fabrication, and increasing precision. Traditional compliant joints are usually limited to relatively small bending angles, as they introduce geometric nonlinearities and accumulate stress concentrations as the deflection increases [60]. Our traveling-wave mechanism prevents stress concentrations, as the traveling wave undergoes relatively stable deformation across 270°. The current 270° limitation stems from the planar heat-pressing fabrication process, which introduces a seam and disrupts the otherwise continuous ring structure of the VS-belt. Seamless fabrication of the VS-belt, e.g., via 3D heat-forming, could remove this discontinuity and enable full 360° rotation.

The pick-and-place experiment (see Section 3.1) demonstrates stepless 270° rotation, expanding the scope of magnetically-actuated end-effectors to tasks that require large and precise tip rotation, such as grasping and cutting. Unlike conventional mechanical locking devices, which are constrained to discrete engagement positions [61], MAGTWIST enables, in principle, infinitely precise rotation through stepless engagement. This is because the magnetic field strength—and thus the applied torque—can be continuously controlled via the applied current. In practice, however, precision may be influenced by factors such as non-uniform heating, non-uniform magnetic fields, and VS-belt-slider friction. While stick-slip does affect the onset of motion, stopping can be achieved at virtually any angle. Moreover, the close-up view in Video S1 shows no visually discernible stick–slip events, suggesting that major stick–slip effects are likely negligible under the tested conditions.

As an end-effector, MAGTWIST uses rotation and subsequent locking to reorient its magnetic moment, thereby enabling diverse magnetization profiles along a manipulator's length. This capability supports in situ shape transitions, allowing intricate 2D and 3D configurations (see Section 3.2). Without a dedicated rotational DOF, a reorientation of the magnet moment would require complex electromagnetic setups to generate highly localized fields for each magnet, which does not exist for clinical in vivo applications. By contrast, MAGTWIST can operate under uniform magnetic fields, simplifying external field requirements, pointing toward new directions in magnetic manipulator actuation.

The combination of precise tip rotation and adaptable shaping provides access to hard-to-reach surgical sites and enables demanding tasks, as demonstrated in the simulated myomectomy (see Section 3.3). In this procedure, magnetically induced S- and C-shapes minimize interaction with the environment during target access, while tip rotation drives the myoma screw for target retraction. The integration of a camera and biopsy tool further underlines MAGTWIST's versatility.

Future developments of MAGTWIST will focus on extending the rotational range to 360° and transitioning to metal-based manufacturing. In addition, integrating functions such as irrigation and suction, along with real-time feedback on force, shape, and temperature, will enable closed-loop control and pre-clinical (ex vivo) testing.

5 | Experimental Section

5.1 | Materials and Fabrication of the VS-belt

To fabricate the heating element of the VS-belt, a thin foil (20 µm in thickness) made of stainless steel (material no. 1.4301) with an electrical resistance of 0.072×10^{-6} Ωm and thermal conductivity of 16.2 W m^{-1} K^{-1} at 20°C is used to achieve high-resistance. A serpentine path is cut into the foil using a laser-cutter (Speedy 300, Trotec Laser, Austria) to increase the resistivity and uniform heat distribution. This serpentine path forms an electrical circuit loop with a resistance of 8 Ω at 20°C. The heating element is placed between two 3D-printed (fused deposition modeling) sheets of polylactic acid filament (Ultimaker PLA, 2.85 mm, MakerPoint, Netherlands) to form the 3-layered VS-belt. The layers are then bonded together via heat pressing for 5 s at 170°C. This creates a planar flexure that is then submerged in water above (T_g) to shape it into a ring. The anchor is thinly coated with high-temperature resin (RS-F2-HTAM-02, Formlabs, United States) and cured using UV-C light for 30 min at 50°C to ensure rigidity during MAGTWIST actuation. Afterward, 100 mm electrical wires for the power supply are connected to the heating element. To prevent cable tension, a slack length is provided.

5.2 | Materials and Fabrication of MAGTWIST

A diametrically magnetized ring magnet (HKCM Europe, grade N40, 318~kJ m^{-3}, outer diameter 8 mm, inner diameter 4 mm, length 9 mm) with an internal flux density of 1.25 T is used to assemble MAGTWIST. The end cap, as well as the inner and outer shaft, are 3D-printed on a Stratasys J750 3D printer (Stratasys, United States) using transparent PolyJet photopolymer (VeroClear, Stratasys, United States). The continuum bellows tubes are fabricated from a semi-flexible composite (Agilus30–VeroClear, Stratasys, United States; Shore A90). The helical structure embedded within the bellows is designed to enhance torsional rigidity and has a pitch of 7.5 mm. It is fabricated from a stiffer variant of the Agilus30-VeroClear composite and exhibits an elongation at break of 30%.

5.3 | Measurement of Reaction Moment

A 6-axis force/torque transducer (ATI Industrial Automation, NANO 43, Apex, NC, USA) is employed to measure the reaction moment, operating at an RDT (rate data transmission) of 7000 Hz with a 5 Hz sensor filter applied. The sensor remains stationary during all tests. For statistical reliability, each measurement is repeated three times.

5.4 | Helmholtz Coil Setup

An electromagnetic coil setup is used for the design validation, the shape reconfiguration demonstration, and the myomectomy demonstration. It is capable of generating a maximum magnetic field of 55 mT in any spatial direction within a cylindrical workspace with equal radius and height of 65 mm [62]. The magnetic field strength and orientation are controlled by regulating the currents in each coil.

5.5 | Thermal Characterization

Thermal measurements in air are made using an infrared camera (Ti400, Fluke Corporation, United States) that is placed 150 mm from MAGTWIST. The measurement data are processed using FLIR ResearchIR software, then analyzed and displayed using MATLAB R2023. MAGTWIST is passively cooled at room temperature between each measurement. In-water measurements are obtained using a 1 mm diameter K-type thermocouple connected to a thermocouple-to-digital converter module (Diligent Pmod TC1, RS PRO, 134-6476) and an Arduino Nano during resistive Joule heating ($t \in [0, 20]$ s) and passive cooling ($t \in [180, 220]$ s). The thermocouple is positioned inside the undulation of MAGTWIST and replaces the center slider of the outer shaft. Three measurements are collected for each applied current of 0.6, 0.7, 0.8, 0.9, and 1.0 A in air, corresponding to powers of 2.88, 3.92, 5.12, 6.48, and 8.00 W, respectively. For 2.5 A in water, the power output corresponds to 50.0 W.

5.6 | Thermomechanical Characterization

The thermomechanical properties of the PLA are characterized using dynamic mechanical analysis with an EPLEXOR 2000 system (Gabo Qualimeter Testanlagen GmbH). The test involves applying a static preload to the samples, followed by sinusoidal mechanical vibrations at a frequency of 1 Hz. The temperature is incrementally increased from 0°C to 80°C at a rate of 2.5°C per minute. This method enables the evaluation of the PLA's elastic modulus as a function of temperature and strain rate.

5.7 | Finite Element Analysis

The reaction moment of MAGTWIST is simulated using COMSOL Multiphysics 6.0 (COMSOL AB, Stockholm, Sweden), employing the Structural Mechanics module in combination with the Nonlinear Structural Materials module. The influence of design parameters on the reaction moment is explored via a parametric sweep in which each design parameter is varied individually. The VS-belt is modeled as a hyperelastic material (Neo-Hookean model), with temperature-dependent material data obtained from dynamic mechanical analysis implemented via interpolation functions in the Materials module to model nonlinear softening effects of the VS-belt. Boundary conditions consist of a fixed constraint to the anchor of the VS-belt, a fixed constraint to the inner shaft, and a prescribed 270° rotation to the outer shaft with a ramp factor of 0.001 to ensure smooth loading. Inertia effects are neglected, and out-of-plane deformations are assumed minimal, allowing the simulation to be performed within a stationary study framework (quasi-static conditions). Meshing is performed using a free triangular mesh with an element size of 0.05 mm, combined with boundary layer elements along the circumference of the VS-belt to capture near-surface effects. The model is analyzed in 2D to improve computational efficiency, leveraging the rotational symmetry of MAGTWIST. Sliding contact between the VS-belt and the shafts is modeled using a penalty method within a quasi-static equilibrium sequence using a Coulomb friction coefficient of 0.6. The nonlinear solver is configured using the double-dogleg method, with a direct solver (MUMPS) employed for the system of equations.

5.8 | Validation of Magnetic Model

The torque between the magnets is evaluated in a magnetostatic FEA using COMSOL Multiphysics 6.0 with the Magnetic Fields, No Currents physics interface. A free tetrahedral mesh with a size of 0.5 mm is applied within a cylindrical coordinate system, and a parametric sweep is conducted in 1 mm increments to assess the magnetic interaction. A testing apparatus is designed to evaluate the simulation accuracy and measure the torque between the magnets experimentally. Two neodymium ring magnets (used for MAGTWIST) are held in a coaxial configuration: one magnet is affixed to a torque sensor, and the other is rigidly attached to an acrylic plate mounted on a linear slide. The dipole of the magnets is misaligned by 90° to generate the maximum restoring torque. Measurements are then recorded as the spacing between magnets is gradually increased in 2 mm increments.

5.9 | Demonstration of Sequential Tip Rotation

MAGTWIST is connected to a robotic arm (Kuka LBR IIwa-14 R820, Augsburg, Germany). A customized compliant gripper is printed on a Stratasys J750 3D printer from transparent VeroClear, with compliant flexures made from the semi-flexible Agilus30–VeroClear composite (Shore A90). MAGTWIST rotation is achieved using a N45 neodymium square magnet (length 120 mm, width 90 mm, thickness 20 mm). The robot arm provides the vertical motion, reducing the distance to the external permanent magnet from 130 mm to 50 mm during operation. The gripper is operated manually via a handle. As the target object, a 50 foam beam is used.

5.10 | Demonstration of Shape Reconfiguration

MAGTWIST is mounted on a manipulator and suspended in the Helmholz coil setup, and magnetic fields of ±20 mT are applied to deflect the manipulator.

5.11 | Myomectomy Demonstration

The myomectomy demonstration is conducted within the Helmholtz coil setup. A silicone model, fabricated from Ecoflex 00-20 silicone rubber (Smooth-On, United States), pigmented with red food dye and cured at room temperature for 24 h, is used to mimic an organic structure. Blueberries serve as the target tissue. For endoscopy and biopsy demonstrations, a miniature camera of diameter 0.91 mm (MD-B1000-120-01, Misumi Electronic Corporation, Taiwan) and a spike-free disposable endoscopic biopsy forceps (Jiangsu ATE Medical Technology Co., Ltd., Changzhou, China) are used. To resect the target tissue, a custom-built myomectomy screw is used and affixed to the tip of MAGTWIST using adhesive (LOCTITE 401, Henkel Adhesive Technologies).

5.12 | Control and Power System

To control the actuation and heating currents, a triple-output DC power supply (Aim-TTi EX354RT, Aim-TTi Instruments, UK) is used for all experiments.

Acknowledgments

This research has received funding from the Dutch Research Council (NWO) under Grant 19220.

Conflicts of Interest

The authors declare no conflicts of interest.

Data Availability Statement

The data supporting the findings of this study are available from the corresponding author upon reasonable request.

References

1. M. Russo, S. M. H. Sadati, X. Dong, et al., "Continuum Robots: An Overview," *Advanced Intelligent Systems* 5, no. 5 (2023): 2200367, https://doi.org/10.1002/aisy.202200367.

2. P. L. Anderson, R. A. Lathrop, and R. J. Webster, "Robot-Like Dexterity Without Computers and Motors: A Review of Hand-Held Laparoscopic Instruments With Wrist-Like Tip Articulation," *Expert Review of Medical Devices* 13, no. 7 (2016): 661–672, https://doi.org/10.1586/17434440.2016.1146585.

3. S. Awtar, T. T. Trutna, J. M. Nielsen, R. Abani, and J. Geiger, "FlexDex™: A Minimally Invasive Surgical Tool With Enhanced Dexterity and Intuitive Control," *Journal of Medical Devices* 4, no. 3 (2010): 037535, https://doi.org/10.1115/1.4002234.

4. M. E. Rosheim, "On a New 10-Millimeter Surgical Robot Wrist," in *Proceedings of the IEEE International Conference on Robotics and Automation (ICRA)* (2022), 7657–7663, https://doi.org/10.1109/ICRA46639.2022.9812073.

5. H. M. Le, T. N. Do, and S. J. Phee, "A Survey on Actuators-Driven Surgical Robots," *Sensors and Actuators A: Physical* 247 (2016): 323–354, https://doi.org/10.1016/j.sna.2016.06.010.

6. J. Sikorski, I. Dawson, A. Denasi, E. E. G. Hekman, and S. Misra, "Introducing BigMag: A Novel System for 3D Magnetic Actuation of Flexible Surgical Manipulators," in *Proceedings of the IEEE International Conference on Robotics and Automation (ICRA)* (2017), 3594–3599, https://doi.org/10.1109/ICRA.2017.7989413.

7. D. Chathuranga, P. Lloyd, J. H. Chandler, R. A. Harris, and P. Valdastri, "Assisted Magnetic Soft Continuum Robot Navigation via Rotating Magnetic Fields," *IEEE Robotics and Automation Letters* 9, no. 1 (2024): 183–190, https://doi.org/10.1109/LRA.2023.3331292.

8. J. Sikorski, S. Mohanty, and S. Misra, "MILiMAC: Flexible Catheter With Miniaturized Electromagnets as a Small-Footprint System for Microrobotic Tasks," *IEEE Robotics and Automation Letters* 5, no. 4 (2020): 5260–5267, https://doi.org/10.1109/LRA.2020.3004323.

9. J. J. Huaroto, M. Richter, M. Malafaia, et al., "MagNeed: Needle-Shaped Electromagnets for Localized Actuation Within Compact Workspaces," *IEEE Robotics and Automation Letters* 8, no. 6 (2023): 3907–3914, https://doi.org/10.1109/LRA.2023.3273519.

10. A. J. Petruska and B. J. Nelson, "Minimum Bounds on the Number of Electromagnets Required for Remote Magnetic Manipulation," *IEEE Transactions on Robotics* 31, no. 3 (2015): 714–722, https://doi.org/10.1109/TRO.2015.2424051.

11. S. Frieler, S. Misra, and V. K. Venkiteswaran, "Selectively Tunable Joints With Variable Stiffness for a Magnetically-Steerable 6-DOF Manipulator," *IEEE Transactions on Medical Robotics and Bionics* 6, no. 4 (2024): 1713-1725, https://doi.org/10.1109/TMRB.2024.3464668.

12. J. Zhang, H. W. Guo, J. Wu, Z. M. Kou, and A. Eriksson, "Design of Flexure Revolute Joint Based on Compliance and Stiffness Ellipsoids," *Proceedings of the Institution of Mechanical Engineers, Part G: Journal of Aerospace Engineering* 236, no. 4 (2022): 623–635, https://doi.org/10.1177/09544100211016978.

13. X. Li, H. Zhu, W. Lin, W. Chen, and K. H. Low, "Structure-Controlled Variable Stiffness Robotic Joint Based on Multiple Rotary Flexure Hinges," *IEEE Transactions on Industrial Electronics* 68, no. 12 (2021): 12452–12461, https://doi.org/10.1109/TIE.2020.3044795.

14. J. R. Cannon, and L. L. Howell, "A Compliant Contact-Aided Revolute Joint," *Mechanism and Machine Theory* 40, no. 11 (2005): 1273–1293, https://doi.org/10.1016/j.mechmachtheory.2005.01.011.

15. D. F. Machekposhti, N. Tolou, and J. L. Herder, "A Review on Compliant Joints and Rigid-Body Constant-Velocity Universal Joints Toward the Design of Compliant Homokinetic Joints," *Journal of Mechanical Design* 137, no. 3 (2015): 032301, https://doi.org/10.1115/1.4029318.

16. M. L. García-Jiménez, L. Castro-Díez, J. Aguirrezabalaga-González, and J. F. Noguera-Aguilar, "Robotic-Like Suturing With FlexDex Surgical System® for Difficult Laparoscopic Suture," *Cirugia Española (English Edition)* 99, no. 3 (2021): 222–228, https://doi.org/10.1016/j.cireng.2021.02.023.

17. C. Forbrigger, E. Fredin, and E. Diller, "Evaluating the Feasibility of Magnetic Tools for the Minimum Dynamic Requirements of Microneurosurgery," in *Proceedings of the IEEE International Conference on Robotics and Automation (ICRA)* (2023), 4703–4709, https://doi.org/10.1109/ICRA48891.2023.10160840.

18. R. E. Dixon, S. J. Hwang, B. H. Kim, K. M. Sanders, and S. M. Ward, "Myosalpinx Contractions Are Essential for Egg Transport Along the Oviduct and Are Disrupted in Reproductive Tract Diseases," In *Smooth Muscle Spontaneous Activity: Physiological and Pathological Modulation,Advances in Experimental Medicine and Biology*, ed. H. Hashitani, R. J. Lang, vol. 1124 (Springer, Singapore, 2019), 265–294, https://doi.org/10.1007/978-981-13-5895-1.

19. S. Sharma, L. C. Jung, N. Lee, et al., "Wireless Peristaltic Pump for Transporting Viscous Fluids and Solid Cargos in Confined Spaces," *Advanced Functional Materials* 34, no. 12 (2024): 2405865, https://doi.org/10.1002/adfm.202405865.

20. M. D. Sinnott, P. W. Cleary, and S. M. Harrison, "Peristaltic Transport of a Particulate Suspension in the Small Intestine," *Applied Mathematical Modelling* 44 (2017): 143–159, https://doi.org/10.1016/j.apm.2017.01.034.

21. L. Xu, R. J. Wagner, S. Liu, et al., "Locomotion of an Untethered, Worm-Inspired Soft Robot Driven by a Shape-Memory Alloy Skeleton," *Scientific Reports* 12 (2022): 12546, https://doi.org/10.1038/s41598-022-16087-5.

22. O. Guetta, D. Shachaf, R. Katz, and D. Zarrouk, "A Novel Wave-Like Crawling Robot Has Excellent Swimming Capabilities," *Bioinspiration & Biomimetics* 18, no. 2 (2023): 026009, https://doi.org/10.1088/1748-3190/acb1e8.

23. Q. Ji, and A. Song, "Bionic Snail Robot Enhanced by Poroelastic Foams Crawls Using Direct and Retrograde Waves," *Soft Robotics* 11, no. 3 (2024): 453–463, https://doi.org/10.1089/soro.2023.0077.

24. L. Zhang, L. Chen, L. Xu, H. Zhao, R. Wen, and F. Xia, "Gastrointestinal-Peristalsis-Inspired Hydrogel Actuators for NIR-Controlled Transport of Viscous Liquids," *Advanced Materials* 35, no. 30 (2023): 2212149, https://doi.org/10.1002/adma.202212149.

25. Y. Qi, J. Shao, Y. Zhao, et al., "A Pneumatic Flexible Linear Actuator Inspired by Snake Swallowing," *Advanced Science* (2024): 2405051, https://doi.org/10.1002/advs.202405051.

26. F. Esser, T. Masselter, and T. Speck, "Silent Pumpers: A Comparative Topical Overview of the Peristaltic Pumping Principle in Living Nature, Engineering, and Biomimetics," *Advanced Intelligent Systems* 1, no. 2 (2019): 1900009, https://doi.org/10.1002/aisy.201900009.

27. J.-B. Chossat and H. Shea, "Permanently Magnetized Elastomer Rotating Actuator Using Traveling Waves," *Smart Materials and Structures* 33, no. 7 (2024): 075022, https://doi.org/10.1088/1361-665X/ad54ad.

28. X. Tian, Y. Liu, J. Deng, L. Wang, and W. Chen, "A Review on Piezoelectric Ultrasonic Motors for the Past Decade: Classification, Operating Principle, Performance, and Future Work Perspectives," *Sensors and Actuators A: Physical* 306 (2020): 111971, https://doi.org/10.1016/j.sna.2020.111971.

29. T. Mashimo, S. Toyama, and H. Matsuda, "Development of Rotary–Linear Piezoelectric Actuator for MRI-Compatible Manipulator," *Proceedings of the IEEE/RSJ International Conference on Intelligent Robots and Systems* (2008): 113–118, https://doi.org/10.1109/IROS.2008.4650623.

30. M. Xun, H. Yu, S. Zhang, Q. Chang, J. Deng, and Y. Liu, "A Large-Step Stick-Slip Rotary Piezoelectric Actuator With High Velocity Under Low Frequency and Small Backward Motion," *Smart Materials and Structures* 32, no. 5 (2023): 055002, https://doi.org/10.1088/1361-665X/acc439.

31. Y. Hao, J. Gao, Y. Lv, and J. Liu, "Low Melting Point Alloys Enabled Stiffness-Tunable Advanced Materials," *Advanced Functional Materials* 32, no. 25 (2022): 2201942, https://doi.org/10.1002/adfm.202201942.

32. J. Lussi, M. Mattmann, S. Sevim, et al., "A Submillimeter Continuous Variable Stiffness Catheter for Compliance Control," *Advanced Science* 8, no. 18 (2021): 2101290, https://doi.org/10.1002/advs.202101290.

33. C. Chautems, A. Tonazzini, Q. Boehler, S. H. Jeong, D. Floreano, and B. J. Nelson, "Magnetic Continuum Device With Variable Stiffness for Minimally Invasive Surgery," *Advanced Intelligent Systems* 2, no. 6 (2020): 1900086, https://doi.org/10.1002/aisy.201900086.

34. G. Scalet, "Two-Way and Multiple-Way Shape Memory Polymers for Soft Robotics: An Overview," *Actuators* 9, no. 1 (2020): 10, https://doi.org/10.3390/act9010010.

35. B. Aksoy and H. Shea, "Multistable Shape Programming of Variable-Stiffness Electromagnetic Devices," *Science Advances* 8 (2022): eabk0543, https://doi.org/10.1126/sciadv.abk0543.

36. G. Ehrmann and A. Ehrmann, "3D Printing of Shape Memory Polymers," *Journal of Applied Polymer Science* 138, no. 34 (2021): 50847, https://doi.org/10.1002/app.50847.

37. H. Yuan, Fauroux, J.-C., F. Chapelle, and X. Balandraud, "A Review of Rotary Actuators Based on Shape Memory Alloys," *Journal of Intelligent Material Systems and Structures* 28, no. 14 (2017): 1863–1885, https://doi.org/10.1177/1045389X16682848.

38. X. Yan, D. Huang, and X. Zhang, "A Novel Curvature-Driven Shape Memory Alloy Torsional Actuator," *Review of Scientific Instruments* 85, no. 12 (2014): 126109, https://doi.org/10.1063/1.4904734.

39. C.-C. Lan, J.-H. Wang, and C.-H. Fan, "Optimal Design of Rotary Manipulators Using Shape Memory Alloy Wire Actuated Flexures," *Sensors and Actuators A: Physical* 153, no. 2 (2009): 258–266, https://doi.org/10.1016/j.sna.2009.05.019.

40. Y. Haga, T. Mineta, T. Matsunaga, and N. Tsuruoka, "Micro-Robotic Medical Tools Employing SMA Actuators for Use in the Human Body," *Journal of Robotics and Mechatronics* 34, no. 6 (2022): 1233–1244, https://doi.org/10.20965/jrm.2022.p1233.

41. B. E. Kratochvil, M. P. Kummer, J. J. Abbott, R. Borer, O. Ergeneman, and B. J. Nelson, "OctoMag: An Electromagnetic System for 5-DOF Wireless Micromanipulation," in *Proceedings of the IEEE International Conference on Robotics and Automation (ICRA)* (2010), 1610–1616, https://doi.org/10.1109/ROBOT.2010.5509857.

42. J. Edelmann, A. J. Petruska, and B. J. Nelson, "Magnetic Control of Continuum Devices," *The International Journal of Robotics Research* 36, no. 1 (2017): 68–85, https://doi.org/10.1177/0278364916683443.

43. M. Richter, V. K. Venkiteswaran, and S. Misra, "Multi-Point Orientation Control of Discretely-Magnetized Continuum Manipulators," *IEEE Robotics and Automation Letters* 6, no. 2 (2021): 3607–3614, https://doi.org/10.1109/LRA.2021.3064285.

44. Y. Piskarev, Y. Sun, M. Righi, et al., "Fast-Response Variable-Stiffness Magnetic Catheters for Minimally Invasive Surgery," *Advanced Science* 11, no. 10 (2024): 2305537, https://doi.org/10.1002/advs.202305537.

45. M. Mattmann, Q. Boehler, X. Z. Chen, S. Pané, and B. J. Nelson, "Shape Memory Polymer Variable Stiffness Magnetic Catheters With Hybrid Stiffness Control," in *Proceedings of the IEEE/RSJ International Conference on Intelligent Robots and Systems (IROS)* (2022): 9589–9595, https://doi.org/10.1109/IROS47612.2022.9981935.

46. H. R. Vanaei, M. Shirinbayan, S. Vanaei, J. Fitoussi, S. Khelladi, A. Tcharkhtchi, "Multi-Scale Damage Analysis and Fatigue Behavior of PLA Manufactured by Fused Deposition Modeling (FDM)," *Rapid Prototyping Journal* 27, no. 2 (2021): 371–378, https://doi.org/10.1108/rpj-11-2019-0300.

47. Y. Piskarev, J. Shintake, C. Chautems, et al., "A Variable Stiffness Magnetic Catheter Made of a Conductive Phase-Change Polymer for Minimally Invasive Surgery," *Advanced Functional Materials* 32, no. 20 (2022): 2107662, https://doi.org/10.1002/adfm.202107662.

48. M. Mattmann, C. De Marco, F. Briatico, et al., "Thermoset Shape Memory Polymer Variable Stiffness 4D Robotic Catheters," *Advanced Science* 9, no. 1 (2022): 2103277, https://doi.org/10.1002/advs.202103277.

49. T. L. Thomas, J. Bos, J. J. Huaroto, V. K. Venkiteswaran, and S. Misra, "A Magnetically Actuated Variable Stiffness Manipulator Based on Deployable Shape Memory Polymer Springs," *Advanced Intelligent Systems* 6, no. 2 (2024): 2200465, https://doi.org/10.1002/aisy.202200465.

50. L. Mao, P. Yang, C. Tian, et al., "Magnetic Steering Continuum Robot Composed of Hard–Soft Hybrid Materials With Programmable Shape and Functionalities," *Nature Communications* 15 (2024): 3759, https://doi.org/10.1038/s41467-024-48058-x.

51. D. Lin, N. Jiao, Z. Wang, and L. Liu, "A Magnetic Continuum Robot With Camber-Controlled Bending Based on Discrete-Magnetized Magnets," *IEEE Robotics and Automation Letters* 6, no. 2 (2021): 3150–3157, https://doi.org/10.1109/LRA.2021.3061376.

52. M. S. D. De La Cruz, and E. M. Buchanan, "Uterine Fibroids: Diagnosis and Treatment," *American Family Physician* 95, no. 2 (2017): 100–107. PMID: 28084714.

53. T. Wang, H. Tang, Z. Xie, and S. Deng, "Robotic-Assisted vs. Laparoscopic and Abdominal Myomectomy for Treatment of Uterine Fibroids: A Meta-Analysis," *Minimally Invasive Therapy & Allied Technologies* 27, no. 5 (2018): 249–264, https://doi.org/10.1080/13645706.2018.1442349.

54. H. Tintara, P. Aiyarak, W. Mitarnun, and A. Geater, "Assessment of the Physical Properties of Laparoscopic Myoma-Fixation Devices," *Surgical Endoscopy* 19, no. 2 (2005): 240–244, https://doi.org/10.1007/s00464-004-9018-3.

55. R. Sano, S. Suzuki, and M. Shiota, "Laparoscopic Myomectomy for the Removal of Large Uterine Myomas," *The Surgery Journal* 6, no. Suppl. 1 (2020): S44–S49, https://doi.org/10.1055/s-0039-1694989.

56. C. He, R. Nguyen, H. Mayer, et al., "Magnetically Actuated Dexterous Tools for Minimally Invasive Operation Inside the Brain," *Science Robotics* 10, no. 100 (2025): eadk4249, https://doi.org/10.1126/scirobotics.adk4249.

57. K. Chinzei, "Safety of Surgical Robots and IEC 80601-2-77: The First International Standard for Surgical Robots," *Acta Polytechnica Hungarica* 16, no. 8 (2019): 59–78, https://doi.org/10.12700/APH.16.8.2019.8.10.

58. M. Milone, P. Anoldo, M. Manigrasso, et al., "Robotic 8-mm Trocar Fascial Wounds: To Close or Not to Close?," *The International Journal of Medical Robotics and Computer Assisted Surgery* 20, no. 2 (2024): e2624, https://doi.org/10.1002/rcs.2624.

59. Q. Ballouhey, P. Clermidi, J. Cros, et al., "Comparison of 8 and 5 mm Robotic Instruments in Small Cavities: 5 or 8 mm Robotic Instruments for Small Cavities?," *Surgical Endoscopy* 32, no. 2 (2018): 1027–1034, https://doi.org/10.1007/s00464-017-5781-9.

60. L. L. Howell, S. P. Magleby, and B. M. Olsen, *Handbook of Compliant Mechanisms* (John Wiley & Sons, Chichester, UK, 2013): 1–516. ISBN 9781119953456, https://doi.org/10.1002/9781118516485.

61. M. Plooij, G. Mathijssen, P. Cherelle, D. Lefeber, and B. Vanderborght, “Lock Your Robot: A Review of Locking Devices in Robotics,” *IEEE Robotics & Automation Magazine* 22, no. 1 (2015): 106–117, https://doi.org/10.1109/MRA.2014.2381368.

62. T. L. Thomas, J. Sikorski, G. K. Ananthasuresh, V. K. Venkiteswaran, and S. Misra, “Design, Sensing, and Control of a Magnetic Compliant Continuum Manipulator,” *IEEE Transactions on Medical Robotics and Bionics* 4, no. 4 (2022): 910–921, https://doi.org/10.1109/TMRB.2022.3204577.

Supporting Information

Additional supporting information can be found online in the Supporting Information section.

Supporting File 1: adfm73560-sup-0001-SuppMat.pdf.
Supporting File 2: adfm73560-sup-0002-VideoS1.mp4.
Supporting File 3: adfm73560-sup-0003-VideoS2.mp4.
Supporting File 4: adfm73560-sup-0004-VideoS3.mp4.
Supporting File 5: adfm73560-sup-0005-VideoS4.mp4.